Middepth Recipes

MASON ROGERS,[a] RAFFAELE FERRARI,[b] AND LOUIS-PHILIPPE NADEAU[c]

[a] *Massachusetts Institute of Technology–Woods Hole Oceanographic Institution Joint Program in Oceanography/Applied Ocean Science and Engineering, Cambridge and Woods Hole, Massachusetts*
[b] *Massachusetts Institute of Technology, Cambridge, Massachusetts*
[c] *Institut des Sciences de la Mer de Rimouski, Rimouski, Quebec*

(Manuscript received 29 October 2022, in final form 20 March 2023, accepted 23 March 2023)

ABSTRACT: The Indo-Pacific Ocean appears exponentially stratified between 1- and 3-km depth with a decay scale on the order of 1 km. In his celebrated paper "Abyssal recipes," W. Munk proposed a theoretical explanation of these observations by suggesting a pointwise buoyancy balance between the upwelling of cold water and the downward diffusion of heat. Assuming a constant upwelling velocity w and turbulent diffusivity κ, the model yields an exponential stratification whose decay scale is consistent with observations if $\kappa \sim 10^{-4}$ m^2 s^{-1}. Over time, much effort has been made to reconcile Munk's ideas with evidence of vertical variability in κ, but comparably little emphasis has been placed on the even stronger evidence that w decays toward the surface. In particular, the basin-averaged w nearly vanishes at 1-km depth in the Indo-Pacific. In light of this evidence, we consider a variable-coefficient, basin-averaged analog of Munk's budget, which we verify against a hierarchy of numerical models ranging from an idealized basin-and-channel configuration to a coarse global ocean simulation. Study of the budget reveals that the decay of basin-averaged w requires a concurrent decay in basin-averaged κ to produce an exponential-like stratification. As such, the frequently cited value of 10^{-4} m^2 s^{-1} is representative only of the bottom of the middepths, whereas κ must be much smaller above. The *decay* of mixing in the vertical is as important to the stratification as its *magnitude*.

SIGNIFICANCE STATEMENT: Using a combination of theory and numerical simulations, it is argued that the observed magnitude and shape of the global ocean stratification and overturning circulation appear to demand that turbulent mixing increases quasi-exponentially toward the ocean bottom. Climate models must therefore prescribe such a vertical profile of turbulent mixing in order to properly represent the heat and carbon uptake accomplished by the global overturning circulation on centennial and longer time scales.

KEYWORDS: Diapycnal mixing; Large-scale motions; Meridional overturning circulation; Budgets; General circulation models

1. Introduction

The stratification of the middepth ocean is an essential ingredient in the buoyancy budget of the deep ocean. Observations reveal that, apart from the polar regions, the vertical profile of the middepth stratification is remarkably exponential, seeming to demand a simple theoretical explanation (Munk 1966). Previous studies of the middepth ocean have proposed such explanations, typically ignoring vertical variation in one or both of two key variables regulating the middepth buoyancy budget: the upwelling velocity and the rate of turbulent mixing (Munk 1966; Munk and Wunsch 1998; Nikurashin and Vallis 2011; Miller et al. 2020). The predictions made by these studies, however, typically disagree with observations of the stratification or observation-based estimates of the vertical structure of the overturning circulation.

The density structure of the Pacific Ocean from the *Hydrographic Atlas of the World Ocean Circulation Experiment (WOCE)* is presented in the top panel of Fig. 1 (Talley 2007). The isopycnals that populate the Pacific middepths, which we define to be beneath the base of the pycnocline at approximately 1-km depth but above the influence of all but the most prominent topography at around 3 km, are strongly sloped in the Southern Ocean but flatten out in the basin to the north. Our focus is on the laterally bounded basin where the stratification is nearly horizontally uniform. The zonally averaged Indo-Pacific middepth stratification, obtained from the WOCE Hydrographic Climatology dataset (Gouretski and Koltermann 2004), is shown in the bottom panels of Fig. 1. At various latitudes, the stratification appears nearly exponential with a decay scale on the order of 1 km.[1] The South Atlantic Ocean has a similar density structure, while departures from an exponential profile are more pronounced in the middepths of the North Atlantic. We will thus focus this study on the Indo-Pacific Ocean and comment on why similar arguments may not apply to the North Atlantic.

In his celebrated "Abyssal recipes" paper, W. Munk attempted to explain the observed quasi-exponential middepth

[1] All exponential fits described in Fig. 1 and hereinafter are linear fits of the natural logarithm of the data. A nonlinear exponential fit of data that span orders of magnitude prioritizes minimizing residuals where the data magnitude is largest and does not accurately capture the exponential structure of the data. Moreover, to assess the linearity of the profile of $\ln(N^2)$ without introducing bias due to the choice of measurement locations, the fit minimizes the integral (rather than sum) of squared residuals. We accordingly define an effective coefficient of determination R^2 by taking the integrated fraction of the variance in the data explained by the fit.

Corresponding author: Mason Rogers, masonr@mit.edu

DOI: 10.1175/JPO-D-22-0225.1

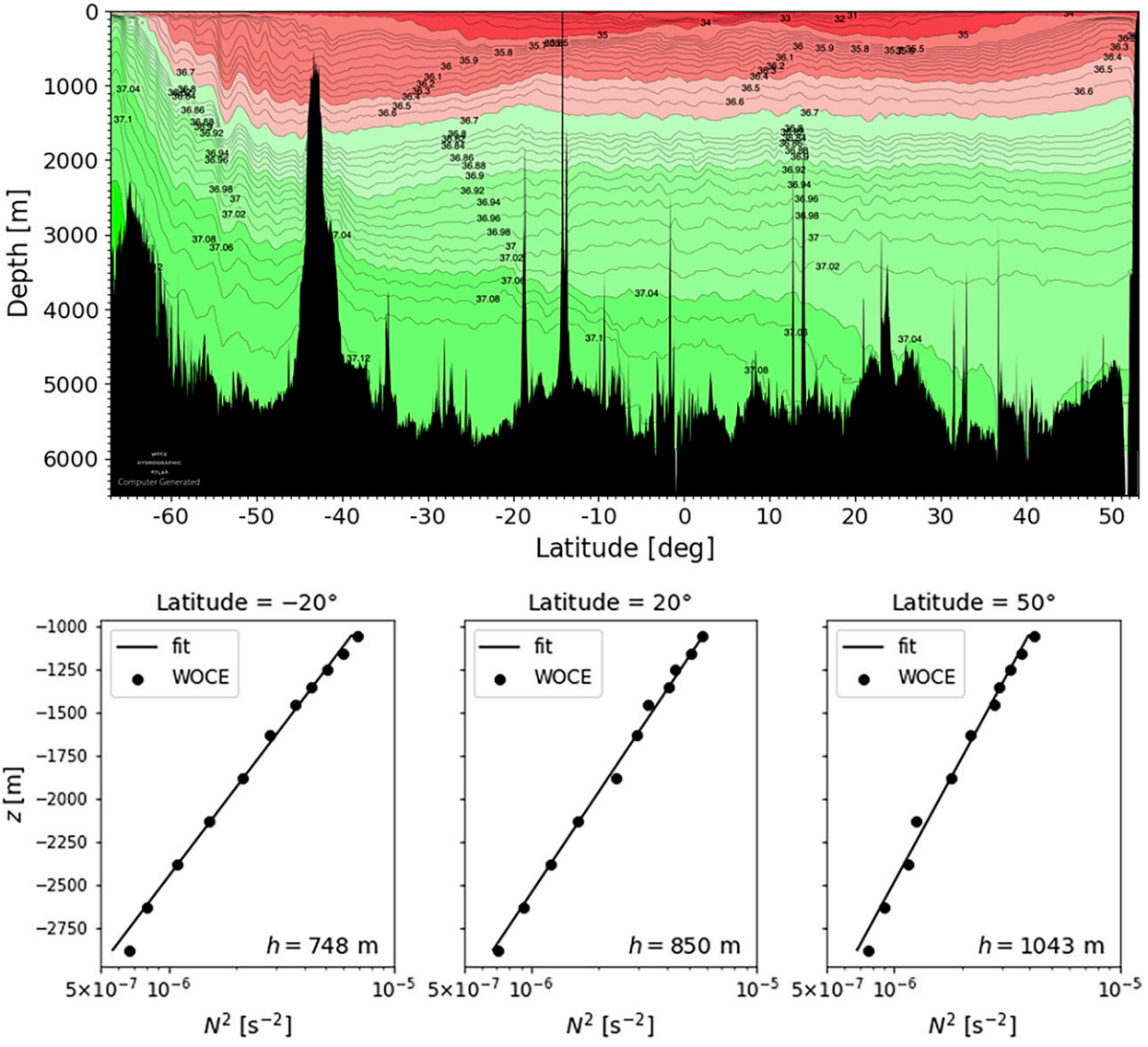

FIG. 1. (top) Potential density referenced to 2000 dbar (σ_2) along 165°W from the WOCE Pacific Ocean Atlas (Talley 2007) section P16. (bottom) Log-scaled, zonally averaged stratification N^2 along three latitudes in the Indo-Pacific (dots) with exponential fits (solid). The *e*-folding scale of each fit is given in the bottom-right corner of each panel, and for every fit the coefficient of determination $R^2 > 0.98$. Stratification is computed with the Gibbs Seawater Package (McDougall and Barker 2011) using data found in the WOCE Hydrographic Climatology dataset (Gouretski and Koltermann 2004).

stratification with a pointwise buoyancy budget balancing the upwelling of cold water with the downward diffusion of heat (Munk 1966). For constant upwelling velocity w and turbulent diffusivity κ, the Munk budget

$$wb_z = \kappa b_{zz} \tag{1}$$

yields an exponential stratification $b_z \propto \exp(wz/\kappa)$. Fitting exponential profiles to the observed stratification to obtain the decay scale $h \equiv \kappa/w$ and using profiles of ^{14}C as a second constraint, Munk determined that observations were consistent with his buoyancy budget if $\kappa \sim 10^{-4}$ m^2 s^{-1}.

Solutions to Eq. (1) depend on the vertical structure of w. Estimates of the Indo-Pacific meridional overturning based on hydrographic profiles suggest that the upwelling velocity varies significantly through the middepths (Talley et al. 2003; Lumpkin and Speer 2007; Rousselet et al. 2021; see Cessi 2019 for a review). Although the location and strength of the maximum upwelling differ among these estimates, all three suggest that the amount of upwelling at 1000-m depth is substantially less than the maximum achieved below. According to Talley et al. (2003), the upwelling at 1000-m depth is about one-third of the maximum value; the more recent estimates suggest there is essentially no upwelling at the top of the middepths. Most relevant to our present work is the robust agreement that the upwelling velocity decreases significantly approaching 1000-m depth from below.

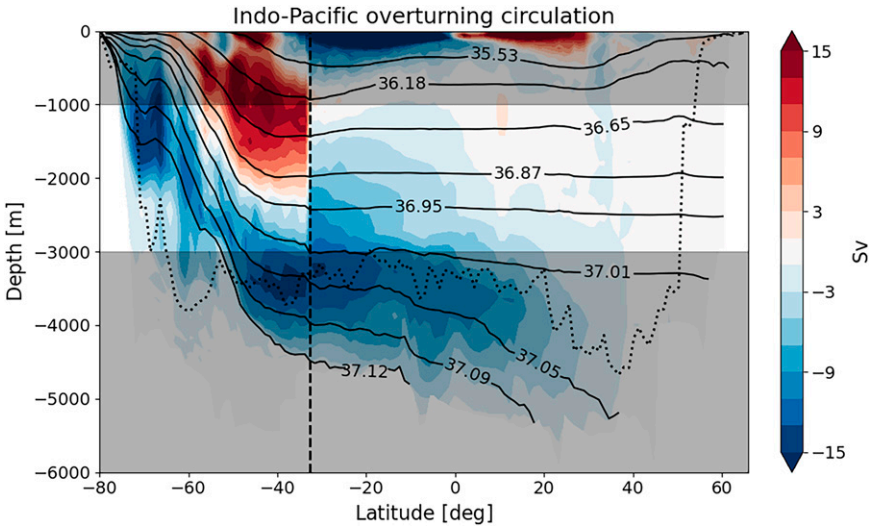

FIG. 2. ECCO consortium estimate of the Southern and Indo-Pacific overturning circulation (Forget et al. 2015; Fukumori et al. 2017) as reported in Rousselet et al. (2021) (color shading), zonally averaged depths of several σ_2 surfaces (solid black lines), and the 25th percentile of ocean depth to indicate the height of the most prominent quartile of topography (dotted black line). The diapycnal transport is computed in σ_2 coordinates for 60 density classes and remapped to the zonally averaged depth of each σ_2 surface. The dashed black line at 33°S distinguishes the Southern Ocean region from the Indo-Pacific basin.

We compute the overturning circulation using the NASA Estimating the Circulation and Climate of the Ocean (ECCO) dataset (Forget et al. 2015; Fukumori et al. 2017). To do so we take the full-run (24 yr) average and integrate the meridional residual volume flux from the seafloor to a collection of σ_2 surfaces, which are then mapped to their zonal-mean depths.[2] The result is plotted in Fig. 2, revealing a maximum transport of ~13 Sv (1 Sv $\equiv 10^6$ m^3 s^{-1}) around 3000-m depth which decays to essentially zero at around 1000 m. The structure of w (which is given by the meridional derivative of the overturning streamfunction) is not consistent with the constant-w assumption in "Abyssal recipes" as pointed out, for example, by Liang et al. (2017). Furthermore, in the upper middepths where $w \approx 0$, Eq. (1) cannot be the leading-order buoyancy balance.

The structure of the meridional overturning in the Atlantic Ocean is very different. The additional sources of dense waters from the Nordic Seas and salty waters from the Mediterranean Sea fuel an additional overturning cell in the middepths stacked on top of the abyssal one found also in the Indo-Pacific (Talley et al. 2003; Lumpkin and Speer 2007; Rousselet et al. 2021). The analysis presented in this paper suggests that this more complicated overturning structure results in a vertical profile of stratification that departs from a simple exponential function. We will therefore focus our study on the Indo-Pacific Ocean. However, the framework developed in this paper applies to any ocean basin, and we plan to apply it to the North Atlantic in future work.

A full theory for the structure of the middepths must predict both w and b_z. An initial attempt at such a theory is due to Gnanadesikan (1999), who formulated a two-layer model of the global ocean to infer the global-mean upwelling across the pycnocline. In this vein Nikurashin and Vallis (2011) extended the model to predict b_z and w for a continuously stratified ocean, matching reentrant channel theories developed for the Southern Ocean meridional overturning circulation with Munk's abyssal recipe in a closed basin (Marshall and Radko 2003; Munk 1966). In the limit of weak turbulent mixing (small κ) the model predicts that the vertical profile of b_z in the closed basin is a mirror image of the meridional gradient b_y at the surface of the reentrant channel, slightly modified by meridional variations in surface winds. This prediction is clearly inconsistent with observed profiles of sea surface buoyancy and zonal wind stress over the Southern Ocean [from, e.g., Orsi and Whitworth (2005) and Lin et al. (2018), respectively], as they would imply a stratification that strengthens with depth. Nikurashin and Vallis (2011) also study the limit of a large, constant diffusivity, but even in this limit, their numerical solutions do not reproduce an exponential-like stratification.

Many others, inspired by microstructure measurements suggesting significant variation in κ (Polzin et al. 1997; Ledwell et al. 2000; St. Laurent et al. 2012; Waterhouse et al. 2014), have attempted to incorporate this variation in theories for the middepths (Munk and Wunsch 1998). However, such efforts have largely ignored the structure in w when connecting theoretical predictions to observations.

[2] Because of zonal variation in the σ_2 field and the domain depth, the zonal-mean depth of σ_2 surfaces is not necessarily a monotonic function of σ_2 even if σ_2 is a monotonic function of z in every column. To impose monotonicity for plotting purposes, we hereinafter adjust the zonal-mean depth of each isopycnal to the maximum zonal-mean depth of all isopycnals of lesser or equal density. This procedure does not affect any numerical calculations, which are performed in buoyancy space before remapping.

Here we construct a variable-coefficient, basin-averaged analog to Munk's pointwise one-dimensional budget and interpret it in the context of observations and solutions to numerical models. We tease apart the relationship between the vertical structures of κ, w, and b_z and obtain constraints on the vertical structure of κ that must hold for the resulting overturning and stratification to be consistent with observations. These constraints suggest that a constant-κ ocean cannot produce a realistic overturning and exponential-like stratification in the middepths regardless of the value of κ.

In section 2 we introduce the variable-coefficient, basin-averaged buoyancy budget and a hierarchy of model configurations for testing it. In section 3 we interpret numerical solutions of these models in light of the basin-averaged buoyancy budget. We conclude by discussing the implications of these results for the vertical structure of the ocean in section 4.

2. Methods

a. Variable-coefficient buoyancy budget

Although the middepth stratification is nearly horizontally uniform, the rates of turbulent mixing and diapycnal upwelling exhibit significant horizontal heterogeneity. A pointwise description of the buoyancy budget therefore depends on fields that vary in all three dimensions and are difficult to measure directly. But a simple and useful one-dimensional budget can be recovered upon averaging the full buoyancy advection–diffusion equation over isopycnals and reinterpreting the upwelling velocity and turbulent diffusivity as isopycnal averages. With minimal additional approximation, the one-dimensional budget can be solved for the stratification while allowing for variation in the isopycnal-average diapycnal velocity and diffusivity.

Various authors have revisited the ideas of "Abyssal recipes" in the context of a variable-coefficient buoyancy budget. We begin following the lead of Walin (1982), Marshall et al. (1999), and Ferrari et al. (2016) to obtain a nearly exact expression for the diapycnal transport in terms of turbulent fluxes.

Ignoring nonlinearities in the equation of state and averaging over spatial scales smaller than a hundred meters and temporal scales shorter than a few hours so that the fluid is stably stratified, the conservation of buoyancy is given by

$$b_t + \mathbf{u}\cdot\nabla b = -\nabla\cdot\mathbf{F}_b. \tag{2}$$

Here $\mathbf{F}_b$ is the turbulent buoyancy flux $\overline{\mathbf{u}'b'}$, where the overbar denotes averaging over the aforementioned scales and primes denote departures from averages. Note that $\mathbf{F}_b$ represents small-scale, unbalanced turbulence (e.g., due to wave breaking) but not larger-scale, balanced turbulence (e.g., due to mesoscale eddies), which is still included in the advection term. Dividing through by $|\nabla b|$ gives the equivalent expression

$$\frac{b_t}{|\nabla b|} + \mathbf{u}\cdot\hat{\mathbf{n}} = -\frac{\nabla\cdot\mathbf{F}_b}{|\nabla b|}. \tag{3}$$

We recognize the left side of Eq. (3) as the diapycnal velocity w_d, which is defined as the difference between the Eulerian velocity normal to an isopycnal ($\mathbf{u}\cdot\hat{\mathbf{n}}$) and the velocity of that isopycnal ($-b_t/|\nabla b|$) (Marshall et al. 1999; Ferrari et al. 2016). We therefore have

$$w_d = -\frac{\nabla\cdot\mathbf{F}_b}{|\nabla b|}. \tag{4}$$

Defining $S(y, b)$ as the portion of the isopycnal with buoyancy b north of latitude y, integrating Eq. (4) over $S(y, b)$ relates the net diapycnal transport across that isopycnal, $\Psi(y, b)$, to the cross-isopycnal turbulent flux:

$$\Psi(y, b) \equiv -\int_{S(y,b)} w_d\, dS = \int_{S(y,b)} \frac{\nabla\cdot\mathbf{F}_b}{|\nabla b|}\, dS. \tag{5}$$

Applying the Reynolds transport theorem (detailed in appendix A) to the last expression recasts the surface integral as an integral over the volume $V(y, b)$ bounded by latitude y to the south, $S(y, b)$ above, and topography below, giving

$$\Psi(y, b) = \frac{\partial}{\partial b}\int_{V(y,b)} \nabla\cdot\mathbf{F}_b\, dV. \tag{6}$$

The boundaries of $V(y, b)$ may include the bounding isopycnal $S(y, b)$, portions of the sea surface where $S(y, b)$ outcrops, portions of the seafloor, and the surface of constant latitude y. We apply the divergence theorem to Eq. (6) and make a few mild assumptions to neglect the contributions due to the sea surface, the seafloor, and the surface of constant latitude y. We first assume that $S(y, b)$ does not outcrop at the surface north of latitude y, which is true for isopycnals in the middepth Indo-Pacific basin. Isopycnals may intersect the seafloor, but we neglect geothermal heating and accordingly any buoyancy fluxes through the ocean bottom. Last, recognizing that mesoscale turbulence is accounted for in Ψ, we parameterize the remaining small-scale turbulent flux $\mathbf{F}_b$ diffusively via $\mathbf{F}_b = -\kappa\nabla b$, which we approximate by its vertical component $\mathbf{F}_b \approx -\kappa(\partial b/\partial z)\hat{\mathbf{z}}$. This is justifiable where vertical buoyancy gradients are much larger than horizontal ones, that is, in most of the ocean except possibly along bottom boundary layers, which occupy too small of an area in the middepths to be a significant contributor to the total diffusive buoyancy flux through $S(y, b)$. We thus obtain

$$\Psi(y, b) = -\frac{\partial}{\partial b}\int_{S(y,b)} \frac{\kappa}{(\partial z/\partial b)}\, dS, \tag{7}$$

providing a relationship between the upwelling across $S(y, b)$ and the mean stratification over $S(y, b)$.

Equation (7) can be inverted to obtain an exact expression for $\partial b/\partial z$, appropriately averaged, as presented in appendix B. For the developments of this paper, it suffices to solve Eq. (7) under the assumption that middepth isopycnals are flat in the basin, so $\partial z/\partial b$ does not depend on x or y and the denominator can be pulled out of the integrand.[3] This assumption will be

[3] Although isopycnals do bend in thin bottom boundary layers, such layers only compose a small fraction of the total area of middepth isopycnals. Ignoring the decrease in b_z and $\mathbf{F}_b$ over this small percentage of the area of $S(y, b)$ results in overestimating the total diffusive flux across $S(y, b)$ by a similarly small and ultimately inconsequential percentage (McDougall and Ferrari 2017).

vindicated by the success of Eq. (10) in describing the model solutions. Moreover, in practice, performing the exact computation presented in appendix B with gridded model output requires many interpolations, often introducing more inaccuracy than making the flat-isopycnal approximation does. We therefore pull the denominator out of the integrand in Eq. (7), leaving

$$\Psi(y, b) = -\frac{\partial}{\partial b}\left[\frac{1}{(\partial z/\partial b)}\int_{S(y,b)} \kappa \, dS\right]. \tag{8}$$

Multiplying through by $\partial b/\partial z$ to rewrite Eq. (8) in z coordinates yields the ordinary differential equation

$$\Psi\frac{\partial b}{\partial z} = -\frac{\partial}{\partial z}\left(\frac{\partial b}{\partial z}\langle\kappa\rangle A\right), \tag{9}$$

where $\langle\kappa\rangle$ denotes the area average of κ over $S(y, b)$ and A denotes the surface area of $S(y, b)$. Equation (9) may be solved for b_z in terms of $b_z(z_0)$ for some depth z_0. The solution is

$$\frac{\partial b}{\partial z} = \frac{\partial b}{\partial z}\bigg|_{z=z_0} \frac{(\langle\kappa\rangle A)|_{z=z_0}}{\langle\kappa\rangle A} \exp\left(-\int_{z_0}^{z} \frac{\Psi}{\langle\kappa\rangle A}\, dz'\right). \tag{10}$$

Note that $-\Psi/A \equiv \langle w_d\rangle$ as defined by Eq. (5) and that Eq. (10) reduces to the Munk solution in the limit of constant κ, w_d, and A.

In general $\partial b/\partial z$ can differ from the stratification N^2 computed from locally referenced potential density due to nonlinearities in the equation of state, which we have neglected. But if b is referenced to a pressure in the middepths (e.g., b is computed from σ_2), we expect that b_z will be very similar to N^2. We therefore flexibly interpret Eq. (10) as an equation for N^2 upon supplying $b_z(z_0) = N^2(z_0)$ as an initial condition for Eq. (9).

Equation (10) relates the stratification, overturning circulation, and turbulent diffusivity of the middepths. Figure 3 suggests how these three pieces fit together to produce an exponential stratification in two demonstrative cases: one in which $\langle\kappa\rangle$ is independent of z and another in which $\langle\kappa\rangle$ is bottom enhanced. Assuming A to be nearly constant for middepth isopycnals due to the small area occupied by seamounts and ridges (see Fig. 2), the vertical profile of the stratification is set by the profiles of $\langle\kappa\rangle$ and Ψ. For constant $\langle\kappa\rangle$, Ψ would have to be independent of buoyancy for N^2 to appear exponential. This hypothesis was explored by Munk (1966), but a constant Ψ is inconsistent with modern estimates as depicted in Fig. 2. If instead $\langle\kappa\rangle$ is bottom enhanced, an exponential stratification can arise as long as Ψ decays toward the surface, consistent with available estimates. We will see evidence of each of these regimes in the numerical solutions presented in section 3.

b. Idealized numerical simulations

We wish to probe the relationship between N^2, Ψ, and $\langle\kappa\rangle$ in Eq. (10) using the output of models of increasing complexity. Our first test bed is an idealized rectangular domain consisting of a laterally bounded basin connected to a reentrant channel, similar to the configuration used by Wolfe and Cessi (2009) and Munday et al. (2013) but at a much coarser resolution. We think of the channel and basin regions as idealized representations of the Southern and Indo-Pacific Oceans respectively.

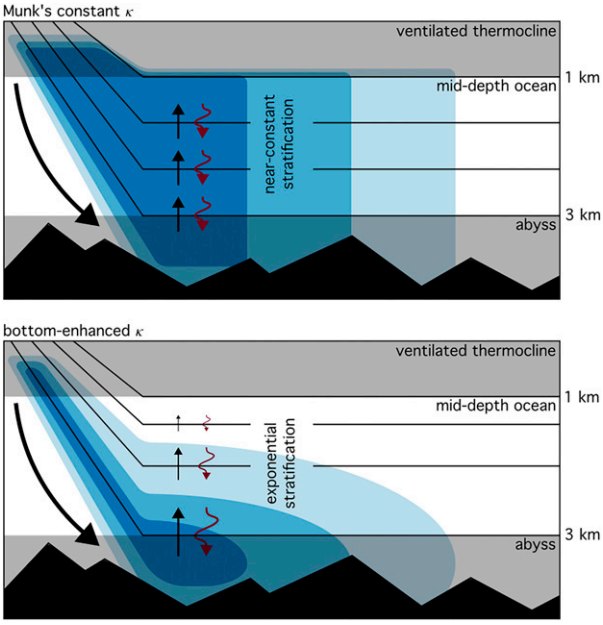

FIG. 3. Schematics of the middepth circulation (blue cells) and isopycnals (black lines) for (top) a large, constant value of κ as hypothesized in "Abyssal recipes" and (bottom) a bottom-enhanced profile of κ as suggested by observations. The magnitude of κ is represented by the lengths of the squiggly red arrows, the magnitude of upwelling velocities is shown by the lengths of the straight black arrows, and the stratification is indicated by the spacing of the isopycnals. The strength of the diapycnal upwelling is given by the gradient of the streamfunction along an isopycnal. In the constant-κ case, the overturning cell is unrealistically broad with upwelling velocities that do not decrease through the middepths. Consequently, the decay scale of the stratification is far longer than observed. In the bottom-enhanced case, the upwelling velocity varies in response to the variation in κ, resulting in an exponential-like stratification characterized by the clustering of isopycnals near the top of the middepths.

The idealized model is intended to distill the minimal set of ingredients necessary to reproduce important large-scale qualitative features of the Indo-Pacific Ocean: isopycnals that plunge from the surface moving north through the Southern Ocean before flattening out in the Indo-Pacific basin, a single overturning cell consisting of deep water sinking in the channel and upwelling throughout the basin, and a stratification that decays quasi exponentially with depth (at least for appropriate choices of parameters). Figure 4 sketches the model setup.

We implement the idealized model in the MITgcm (Marshall et al. 1997). The domain is 20° wide with a reentrant channel spanning from 68° to 48°S and a vertically walled basin from 48°S to 68°N. The domain is 4 km deep with a flat bottom. The model has a horizontal resolution of 2° × 2° and 40 vertical levels with resolution stretching from 37 m at the surface to 159 m at the bottom.

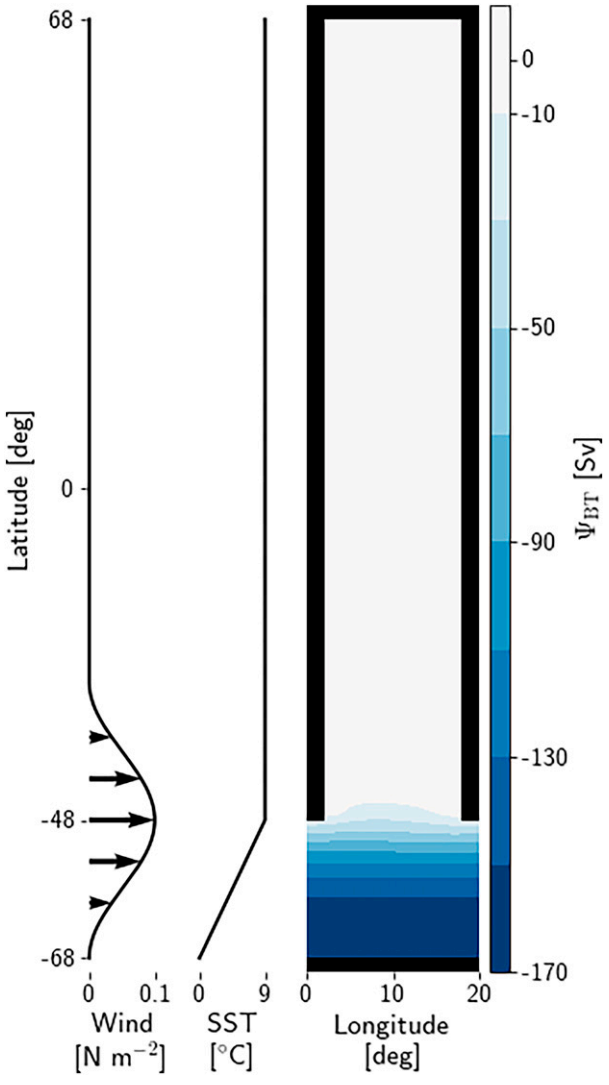

FIG. 4. (left) Surface wind stress, (center) restoring sea surface temperature, and (right) model geometry for the idealized model with a maximum wind stress $\tau = 0.1$ N m^{-2}. The barotropic streamfunction for the variable-κ configuration described in section 3a is plotted in color on the right to give a sense of the horizontal circulation, which is generally zonally symmetric apart from a small meander of the channel current into the basin.

Such a coarse, idealized configuration requires parameterizations of several unresolved processes. Small-scale turbulent diffusion is parameterized with a diapycnal diffusivity κ, variation of which is one of the centerpieces of this study. The effect of baroclinic eddies on the large-scale circulation is represented with a Gent–McWilliams closure, which sets the rate at which isopycnals slump via a diffusivity K_{GM} times the local isopycnal slope (Gent and McWilliams 1990). We set $K_{GM} = 1000$ m^2 s^{-1} unless otherwise stated. The eddy-induced circulation is tapered for isopycnals with slope steeper than 10^{-2} via a scheme introduced by Gerdes et al. (1991). Without topography, form drag must be parameterized; we apply a linear bottom drag coefficient of 6.5×10^{-5} s^{-1}. Last, turbulent convection is represented with a convective adjustment scheme.

For thermodynamics we employ a linear equation of state $\rho = \rho_0(1 - \alpha T)$. The idealized configuration does not feature an independent salinity variable or sea ice. Thus, buoyancy is linearly proportional to temperature $b = g\alpha T$, and ρ is best thought of as a potential density since it does not depend on pressure. We apply idealized wind and thermal forcing inspired by the surface forcing acting on the real ocean. The wind stress is purely zonal, peaking at the channel–basin boundary and vanishing north of 28°S. This profile is broadly consistent in magnitude and shape (e.g., the location of the peak and meridional extent) with the stress exerted by the Southern Hemisphere westerlies over the Southern Ocean, but it does not drive strong near-surface gyres in the narrow basin domain. We justify the absence of wind forcing in the basin by noting that the isopycnals that occupy the middepths of the Indo-Pacific basin are not exposed to wind-driven forcing, which only penetrates down to the depths of the pycnoclines or 500–1000 m. The sea surface temperature is restored to a profile that increases linearly with latitude from 0° to 9°C over the channel and remains constant at 9°C over the basin. The temperature range is chosen such that the corresponding potential density range agrees with that observed in the middepth Indo-Pacific. The meridional temperature/potential density profile at the channel surface agrees with observations over the Southern Ocean and is clearly distinct from the quasi-exponential vertical structure observed in the middepth Indo-Pacific basin. The restoring temperature is kept constant north of the channel to suppress any circulation in the upper ocean, which is not the focus of our study.

The resultant model has two key external parameters: the diapycnal diffusivity κ and the peak wind stress τ. We run the model to equilibrium for many combinations of these parameters. In addition to constant values of κ, we consider bottom-enhanced profiles of κ to capture the enhancement of mixing toward the seafloor reported in microstructure and tracer observations above rough topography (Polzin et al. 1997; Ledwell et al. 2000; St. Laurent et al. 2012; Waterhouse et al. 2014). In particular we use an exponential profile of κ as a function of height above bottom as proposed by St. Laurent et al. (2002). We employ κ profiles of the form

$$\kappa(z) = \kappa_{bg} + (\kappa_0 - \kappa_{bg})e^{-(z+D)/\ell_\kappa}, \tag{11}$$

where κ_{bg} is a background diffusivity away from topography, κ_0 is a much larger value achieved at the bottom of the domain at $z = -D$, and ℓ_κ is the e-folding scale over which mixing decays from κ_0 to κ_{bg}. Typical values for κ_{bg} are on the order of 10^{-5} m^2 s^{-1}, chosen to match the diffusivities observed far from topography (e.g., Ledwell et al. 1998, 2011; Waterhouse et al. 2014).

To test the validity of Eq. (10), we compare the model output N^2 with that reconstructed by applying Eq. (10) to the prescribed κ profile and the model output Ψ. Computation of the overturning transport Ψ is carried out by integrating the meridional residual velocity, that is, the sum of the Eulerian velocity v_E and the eddy-induced velocity parameterized

through the GM parameterization v_{GM}, vertically from the seafloor up to each temperature/buoyancy surface and zonally over the full extent of the domain of length L_x:

$$\Psi(y, b) = -\int_0^{L_x} \int_{b' \le b} (v_E + v_{GM})\, dz\, dx. \tag{12}$$

Here we have expressed Ψ, defined in Eq. (5) as the diapycnal volume flux into $V(y, b)$ from above, as the meridional volume flux out of $V(y, b)$ to the south. In the Indo-Pacific where isopycnals do not outcrop in the basin to the north, the two must be the same in steady state, and Eq. (12) requires fewer interpolations from the model z grid to compute in b coordinates.

The results will be presented as a function of density instead of buoyancy, with $\rho = \rho_0[1 - (b/g)]$, to ease comparison with the more realistic global simulation introduced in section 2c. In the global setup the model uses a nonlinear equation of state, and the analysis must be done in terms of potential density to eliminate dynamically irrelevant compressive effects. In the idealized model the linear equation of state includes no compressive effects and therefore density and potential density are equivalent.

c. Global ocean simulation

In addition to the idealized model, we consider a global ocean simulation with realistic geometry, surface forcing, and bathymetry. The model is designed to capture the salient features of the observed ocean's stratification and overturning while remaining computationally cheap enough to run to equilibrium. (Some notable data products, such as ECCO output, are not sufficiently equilibrated in the deep ocean to study the time-independent budget presented here.) The MITgcm is run with 2.8125° × 2.8125° horizontal resolution and 40 vertical levels decreasing in resolution from 10 m at the surface to 391 m for the bottom grid cell at 5200-m depth. The model uses the Jackett and McDougall (1995) equation of state with nonlinear dependence on temperature, pressure, and salinity. There is no explicit representation of sea ice.

Subgrid-scale physics is parameterized with the same schemes used in the idealized model with some slight changes in parameter values. The linear bottom drag coefficient is set to 10^{-7} s^{-1}, a value much smaller than in the idealized simulations, because the model now includes topographic form drag. The Gent–McWilliams closure for baroclinic instability uses $K_{GM} = 500$ m^2 s^{-1}. In addition, we employ a Redi diffusivity of $K_{Redi} = 1000$ m^2 s^{-1} that mixes temperature and salinity along isopycnals (Redi 1982).

The surface wind stress is taken from Trenberth et al. (1989), linearly interpolating monthly temporal data. Surface forcing of temperature and salt is imposed through a combination of restoring and prescribed fluxes. Temperature and salinity are restored to the surface values from the ECCO version 4 release 3 monthly interpolated climatology (Forget et al. 2015; Fukumori et al. 2017) with piston velocities of 3.2×10^{-6} m s^{-1} and 8.0×10^{-7} m s^{-1}, respectively. An additional surface salt flux equal to the depth-integrated ECCO salt plume flux is added to account for brine rejection during ice formation, a process otherwise missing in a model without ice.

The diffusivity is again an exponentially decaying function of height above bottom given by Eq. (11). We set $\kappa_{bg} = 10^{-5}$ m^2 s^{-1} to ensure numerical noise in the solution is negligible, $\kappa_0 = 8.6 \times 10^{-4}$ m^2 s^{-1} as obtained by averaging the bottom values of Nikurashin and Ferrari (2013), and $\ell_\kappa = 667$ m to obtain an overturning circulation comparable to the cell depicted in Fig. 2. Because the domain depth D depends on x and y, κ varies horizontally as well as vertically in this configuration. Thus, the profile of $\langle\kappa\rangle$ as a function of depth is distinct from the pointwise profile of κ as a function of height above bottom. As evident in Eq. (10), it is the structure of $\langle\kappa\rangle$ that is most important to the basin-average stratification. We will discuss in section 4b the role topography plays in setting the $\langle\kappa\rangle$ profile.

All computations are performed as described for the idealized model with the caveat that zonal integrals are restricted to the Indo-Pacific basin north of 33°S. Because we are primarily interested in the middepths, we conduct our analysis using potential density referenced to 2000 dbar, σ_2, as the density coordinate.

3. Results

a. Idealized simulations

We run the idealized model to equilibrium for various choices of κ and τ. The time required to achieve equilibrium depends on the parameter values but is always on the order of the diffusive time scale D^2/κ, where $D = 4000$ m is the domain depth and κ a typical value. For the subsequent discussion we consider three particularly illustrative examples, each with maximum wind stress $\tau = 0.1$ N m^{-2} but differing in their κ profiles: a constant profile with a value representative of the upper ocean ($\kappa = 2.5 \times 10^{-5}$ m^2 s^{-1}), a constant profile with a value representative of Munk's prediction for the deep ocean ($\kappa = 1.0 \times 10^{-4}$ m^2 s^{-1}), and an exponentially bottom-enhanced profile from Eq. (11) with the same vertically averaged value of 1.0×10^{-4} m^2 s^{-1}. Varying the wind stress affects the depth to which the stratification penetrates but does not alter the central relationship between the diffusivity, stratification, and overturning. In particular larger wind stresses steepen isopycnal slopes in the channel, squishing the overturning cell against the bottom of the domain. We therefore focus on the effects of varying κ for the remainder of our discussion.

For the variable-κ case, the κ profile is imposed as per Eq. (11) with $\kappa_{bg} = 1.0 \times 10^{-5}$ m^2 s^{-1}, $\kappa_0 = 3.89 \times 10^{-4}$ m^2 s^{-1}, and $\ell_\kappa = 964$ m. The value of ℓ_κ is derived from a profile obtained by horizontally averaging at constant depth the three-dimensional dataset of Nikurashin and Ferrari (2013), whose model features topography. We borrow the decay scale of this horizontally averaged profile to mimic the effect of topographic variations on the $\langle\kappa\rangle$ profile in our flat-bottomed model. The value of κ_0 is then chosen such that the vertical average of κ is equal to 1.0×10^{-4} m^2 s^{-1}. This allows us to compare with the strong-constant-κ case, illuminating the role of the structure of κ while controlling for its mean value: the strong-constant-κ and variable-κ cases are representative of the two scenarios illustrated in Fig. 3.

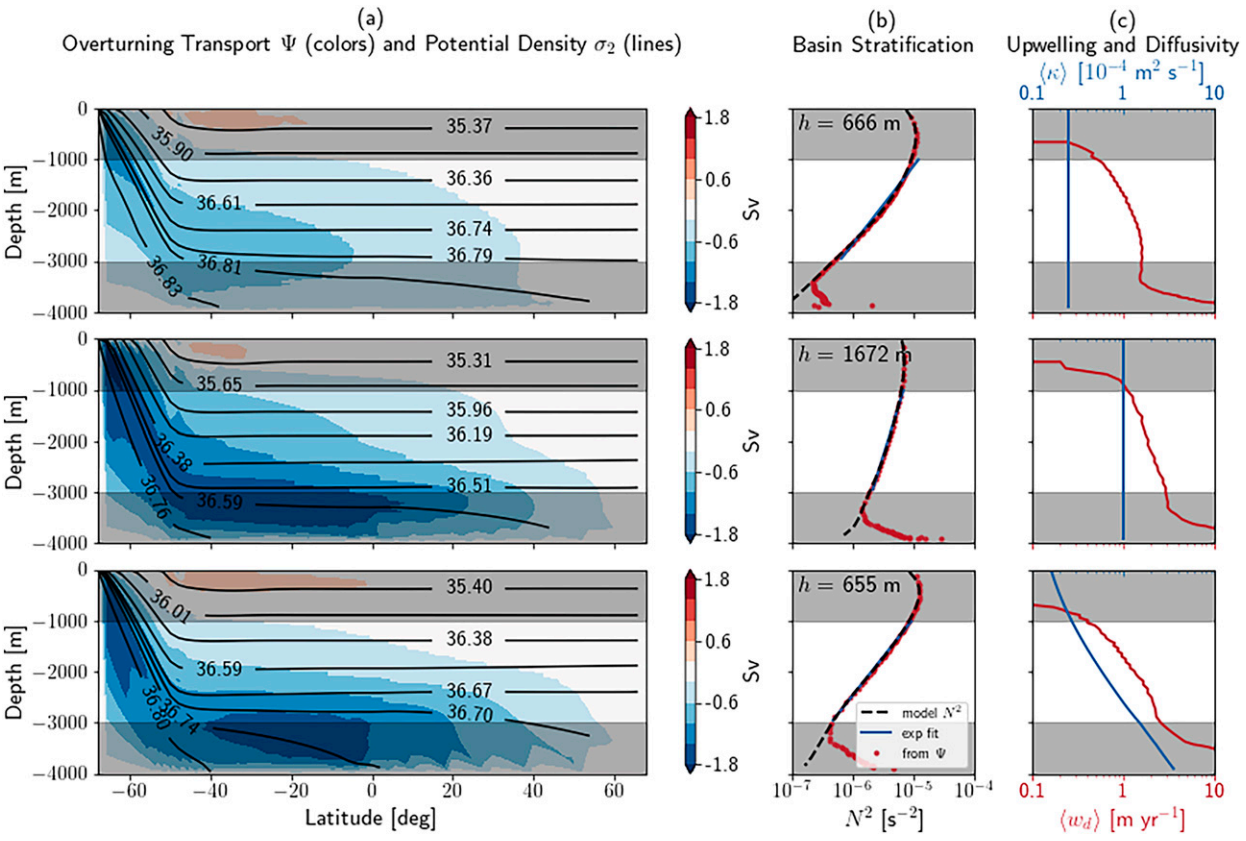

FIG. 5. Equilibrated solutions to the idealized model for (top) $\kappa = 2.5 \times 10^{-5}$ m^2 s^{-1}, (middle) $\kappa = 1.0 \times 10^{-4}$ m^2 s^{-1}, and (bottom) an exponentially bottom-enhanced profile of κ given by Eq. (11) with $\kappa_{bg} = 1.0 \times 10^{-5}$ m^2 s^{-1}, $\kappa_0 = 3.89 \times 10^{-4}$ m^2 s^{-1}, and $\ell_\kappa = 964$ m. For each diffusivity profile, (a) the diapycnal overturning transport Ψ (colors) and the zonally averaged depths of several σ_2 surfaces (black lines) are plotted. We then compare (b) the stratification averaged north of 40°S with an exponential fit between 1- and 3-km depth and a reconstruction of N^2 from Ψ via Eq. (10). The e-folding scale of the exponential fit is printed in the upper-left corner. Also plotted are the (c) isopycnal-average diffusivity and upwelling velocity over the same latitude range.

Solutions for these three configurations are depicted in Fig. 5a. In all three cases, the isopycnals that populate the middepths are flat in the basin and outcrop to the surface in the channel. Only within a kilometer of the bottom do isopycnals bend into the seafloor to enforce the no-buoyancy-flux bottom boundary condition (Mashayek et al. 2015). The overturning circulation for each case consists of a single cell in which deep water forms in the channel, upwells diapycnally in the basin, and returns to the south along isopycnals in the channel. These qualitative features agree with the middepth Indo-Pacific, making these simulations a useful paradigm to study the Indo-Pacific Ocean overturning and stratification. For completeness we show the barotropic horizontal circulation for the variable-κ case in Fig. 4. The dominant horizontal flow represents the Antarctic Circumpolar Current, which is nearly zonally uniform in this idealized configuration. There is hardly any barotropic circulation in the basin where we impose neither a surface stress nor a restoration to a varying surface temperature.

Quantitatively, the vertical profiles of stratification and upwelling (Figs. 5b,c) differ among the three example configurations. The $\kappa = 2.5 \times 10^{-5}$ m^2 s^{-1} case features a weak overturning circulation with maximum transport above the base of the middepths. The stratification decays at a nearly exponential rate with an e-folding scale of 666 m. There is slight visible curvature in the log-space graph of the stratification in Fig. 5, implying a small systematic deviation of the model output from an exponential profile. Nonetheless, an exponential fit returns a coefficient of determination $R^2 = 0.98$, suggesting that the model output agrees with an exponential profile almost as well as observations do, even if the departures from exponential have a more distinct character. Although the stratification is broadly consistent with observations, the overturning cell is weak and not as confined to the abyss as in hydrography-based estimates. Perhaps unsurprisingly, without vigorous mixing to sustain a strong overturning circulation, one cannot recover salient features of observations.

The $\kappa = 1.0 \times 10^{-4}$ m^2 s^{-1} case, that is, the ocean hypothesized by Munk, exhibits a tall overturning cell with significant upwelling across 1000-m depth, akin to the top panel of the schematic in Fig. 3. The stratification decays very slowly with depth with an e-folding scale of 1672 m over the 2000-m middepth range. Neither the stratification nor the overturning circulation is consistent with evidence of an overturning cell that roughly closes at the top of the middepths and a stratification that decays more rapidly through them.

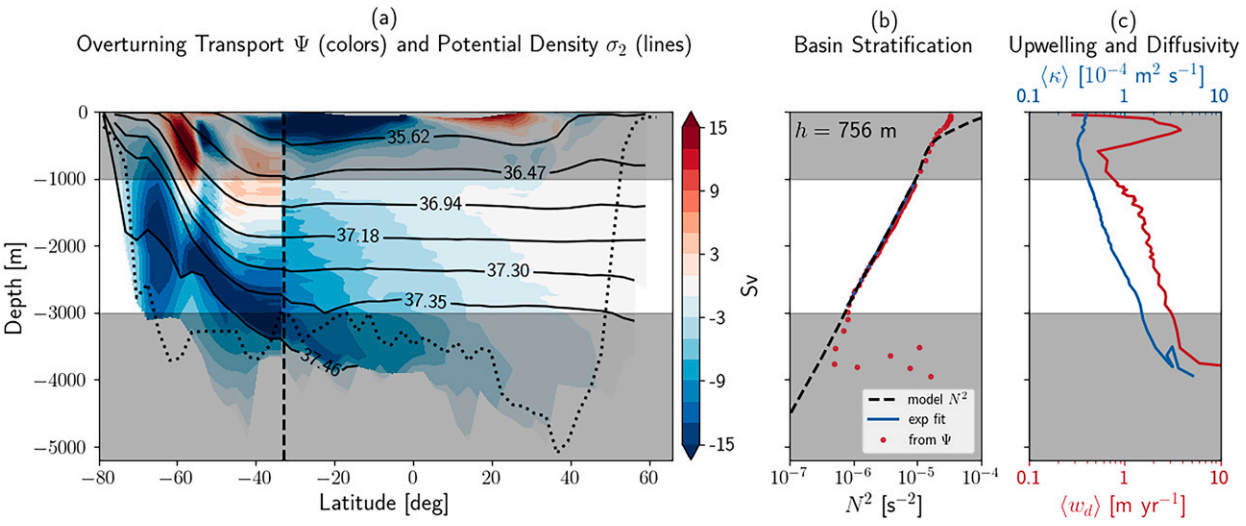

FIG. 6. (a) The diapycnal overturning transport Ψ (colors), zonally averaged depths of several σ_2 surfaces (solid black lines), and the 25th percentile of ocean depth to indicate the height of the most prominent quartile of topography (dotted black line); (b) basin-averaged stratification, fit, and reconstruction via Eq. (10); and (c) the isopycnal-average upwelling and diffusivity. The zonal integrals required to compute the overturning and mean σ_2 surfaces are taken globally south of 33°S and restricted to the Indo-Pacific basin north of 33°S, as indicated by the dashed black line. Basin averages are also taken north of 33°S.

The solution with a bottom-enhanced diffusivity has a strong overturning cell that features a maximum transport below the bottom of the middepths and little upwelling across the pycnocline, much like the bottom panel of Fig. 3. The e-folding scale of the stratification is 655 m ($R^2 > 0.99$), much closer to the values observed in the real Indo-Pacific than in the strong-constant-κ case. In the middepths the upwelling velocity and the diapycnal diffusivity both decay rapidly toward the surface. Judging by both the stratification and the overturning, the variable-diffusivity ocean agrees best with observational evidence.

In section 4 we interpret the results of these three simulations using the relationship between streamfunction and stratification captured by Eq. (10). As a first step we show in Fig. 5b that the basin stratification reconstructed from $\Psi(y, b)$ at $y = 40$°S via Eq. (10) (red dots) matches that directly diagnosed from the model solutions (dashed black lines) in the middepths very well. In particular, the reconstructed N^2 profiles give e-folding scales of 667 m for the weak-constant-κ case, 1654 m for the strong-constant-κ case, and 648 m for the variable-κ case, agreeing with the values computed directly from the model output N^2 profiles to within 2%. The discrepancies that emerge below 3000 m have to do with the bending of isopycnals to match the no-flux bottom boundary conditions, breaking the flat isopycnal assumption invoked to derive Eq. (10). In Fig. 5c, we depict the profiles of $\langle\kappa\rangle$ and $\langle w_d\rangle = -\Psi/A$ from which the stratification is reconstructed. Wherever κ is constant, so too is $\langle\kappa\rangle$, but where κ is bottom enhanced, $\langle\kappa\rangle$ is as well. The rate at which $\langle w_d\rangle$ decays toward the surface within the middepths depends on the $\langle\kappa\rangle$ profile, exhibiting the most significant variation between 1000 and 3000 m in the variable-κ case.

b. Global ocean simulation

The idealized configurations lack variable bathymetry, realistic continent geometry, and a second basin which has northern deep water formation. We therefore repeat the exercise of comparing the stratification obtained from model output with that reconstructed from the overturning circulation in the coarse global configuration, depicted in Fig. 6.

The model solution satisfactorily captures the features of the observed ocean most relevant to assessing Eq. (10). The middepth stratification can hardly be distinguished from an exponential function: an exponential fit returns a value of $R^2 > 0.999$. The fit further returns an e-folding scale of 756 m, within the range of observed values (see Fig. 1). The model overturning cell exhibits its strongest upwelling in the abyss and little upwelling across a depth of 1000 m, much like the overturning cell computed from observations in Fig. 2. The magnitudes are comparable as well, with a maximum transport in the Indo-Pacific middepths of around 12 Sv.

Equation (10) holds in the middepth Indo-Pacific, giving an estimate of $h \approx 746$ m. The discrepancy between this estimate and the directly computed value of 756 m is less than 2% despite neglecting nonlinearities in the equation of state in Eq. (2), making the flat isopycnal approximation in Eq. (8), and interpreting Eq. (10) as a formula for N^2 instead of b_z. The accuracy of the reconstruction falls off in the upper ocean where surface fluxes should be included. [This could be done following Eq. (6) but is not relevant to our work, which focuses on the middepths.] The average upwelling velocity $\langle w_d\rangle$ and diffusivity $\langle\kappa\rangle$ track together through the middepths such that their ratio is nearly constant despite both decaying by a factor of approximately 3.5. We will discuss in section 4a how the covariation of $\langle\kappa\rangle$ and $\langle w_d\rangle$ is key to obtaining exponential solutions to Eq. (10) that reconcile observations of the middepth stratification and estimates of the overturning with theory.

4. Discussion

a. *Sufficient conditions for exponential stratification*

Ignoring variation in the isopycnal area A, which is roughly constant for flat isopycnals above most ridges and seamounts, Eq. (10) implies that if $|\Psi|$ varies from a maximum to zero over the middepths, a constant κ is inconsistent with an exponential stratification. That is, given the observed structure of Ψ, κ must vary significantly to produce an exponential-like stratification.

There are at least two families of $\langle\kappa\rangle$ and Ψ profiles that yield an exponential stratification via Eq. (10). The first case was studied by Munk (1966): κ and $w_d = -\Psi/A$ are independent of z. In this case, the stratification is perfectly exponential with an e-folding scale $h \equiv \kappa/w_d$. Observations suggest that $h \sim 10^3$ m and $w_d \sim 10^{-7}$ m s^{-1}, and Munk's analysis therefore implies $\kappa \sim 10^{-4}$ m^2 s^{-1}. Problematically the value chosen for w_d is somewhat arbitrary because it is taken as the maximum upwelling velocity which occurs at the bottom of the middepths. If a value farther up the water column were chosen, Munk's model would predict a lower κ value. The problem is that the assumption of a constant upwelling velocity over the middepth range is inconsistent with estimates from hydrography that the lower overturning cell closes beneath 1000 m, and the prescription of constant κ is at odds with available observations.

The two idealized simulations with constant diffusivity support the claim that a constant diffusivity cannot generate solutions consistent with observations. In the small-constant-κ case, the diffusivity is too weak to sustain an adequately strong overturning. When κ is increased as necessary to sustain a reasonably strong overturning, the overturning cell extends too far up in the water column. While it is possible that for some constant value of κ the solutions would yield a realistic overturning decaying within the middepths, such a solution would not have an exponential middepth stratification, as can be inferred by substituting a constant κ and variable Ψ into Eq. (10).

A second class of $\langle\kappa\rangle$ and Ψ profiles that produce exponential solutions to Eq. (10) is obtained if $\langle\kappa\rangle$ and $\langle w_d\rangle$ both decay quasi-exponentially moving up through the middepths with e-folding scale $\ell_{\langle\kappa\rangle}$ such that $\langle\kappa\rangle/\langle w_d\rangle$ is nearly constant. In this case, Eq. (10) becomes

$$N^2 = N^2(z_0)\exp\left(\frac{z - z_0}{\ell_{\langle\kappa\rangle}}\right)\exp\left(\frac{z - z_0}{\langle\kappa\rangle/\langle w_d\rangle}\right). \tag{13}$$

The stratification N^2 is the product of two exponentials and is therefore itself an exponential with decay scale

$$h \equiv \frac{\ell_{\langle\kappa\rangle}\langle\kappa\rangle/\langle w_d\rangle}{\ell_{\langle\kappa\rangle} + \langle\kappa\rangle/\langle w_d\rangle}. \tag{14}$$

Note that h is independent of the choice of depth at which $\langle\kappa\rangle$ and $\langle w_d\rangle$ are taken by assumption.

In fact, this second family of exponential solutions generalizes the first. A constant κ corresponds to taking the limit $\ell_{\langle\kappa\rangle} \to \infty$ in Eq. (14), upon which the familiar Munk scaling is recovered in an isopycnal-average sense. One can imagine more contrived $\langle\kappa\rangle$ and Ψ profiles that conspire to produce an exponential stratification, but the two identified thus far serve as helpful archetypes in classifying and understanding different qualitative regimes of model solutions and observations. Additionally, the existence of variable-κ exponential solutions demonstrates how Ψ can be negligibly small at the top of the middepths and $\langle\kappa\rangle$ can span orders of magnitude while still yielding an exponential-like stratification.

The global model (Fig. 6) and the variable-κ configuration of the idealized model (Fig. 5, bottom) feature the offsetting variation in Ψ and $\langle\kappa\rangle$ characteristic of the second class of solutions. In the global model, Ψ and $\langle\kappa\rangle$ increase more than threefold between 1- and 3-km depth at roughly the same rate. Hence their ratio is approximately constant and yields $\langle\kappa\rangle/\langle w_d\rangle \approx 1545$ m with a standard deviation of just 254 m. Moreover, the decay of $\langle\kappa\rangle$ is close to exponential through the middepths with $\ell_{\langle\kappa\rangle} = 1454$ m ($R^2 = 0.98$). Consistent with Eq. (10), the decay of the stratification is nearly exponential. Equation (14) can be used to estimate a decay scale of $h \approx 749$ m, within 1% of the value of 756 m obtained by a fit of the stratification profile. It is worth keeping in mind that the bottom-enhanced κ profile used in our simulations is supported by in situ microstructure profiles which find that κ increases significantly approaching rough, geologically young topography—for example, ridges and seamounts—and only exceeds Munk's value of 10^{-4} m^2 s^{-1} within a few hundred meters of the seafloor (Polzin et al. 1997; Ledwell et al. 2000; St. Laurent et al. 2012; Waterhouse et al. 2014).

A similar analysis applies to the variable-κ case of the idealized model. For that case, the profile of $\langle\kappa\rangle/\langle w_d\rangle$ has a mean value of 1574 m in the middepths with a standard deviation of just 190 m, and the profile of $\langle\kappa\rangle$ decays with an e-folding scale of 1178 m ($R^2 > 0.99$). Together these suggest that the stratification should be close to exponential, which it indeed is. Equation (14) predicts a decay scale of 674 m for N^2, within 3% of the directly computed value of 655 m.

Both hypotheses—constant κ and Ψ and covarying quasi-exponential $\langle\kappa\rangle$ and Ψ—allow for an exponential stratification, but only the latter also admits a strong overturning cell confined to the deep ocean. The discrepancy between state estimates of the overturning circulation and the constant-diffusivity ocean hypothesized by Munk implies that the ocean stratification is set by both the magnitude and the vertical profile of κ. A large enough mixing on average is insufficient to explain the middepth stratification and circulation; the mixing must increase with depth, and it must do so at a particular rate.

b. *The distinction between profiles of κ and $\langle\kappa\rangle$*

Dividing the integrated budget Eq. (9) by $-b_z\langle\kappa\rangle A$ reveals a relationship between the average upwelling velocity and the structures of $\langle\kappa\rangle$, b_z, and A:

$$\frac{\langle w_d\rangle}{\langle\kappa\rangle} = \frac{\langle\kappa\rangle_z}{\langle\kappa\rangle} + \frac{b_{zz}}{b_z} + \frac{A_z}{A}. \tag{15}$$

The terms on the right side are signed inverse height scales characteristic of $\langle\kappa\rangle$, b_z, and A, respectively. For exponential

profiles of $\langle\kappa\rangle$ (decaying with height) and b_z (decaying with depth) with respective e-folding scales $\ell_{\langle\kappa\rangle}$ and h, $\langle\kappa\rangle_z/\langle\kappa\rangle = -1/\ell_{\langle\kappa\rangle}$ and $b_{zz}/b_z = 1/h$. The term A_z/A can be computed directly from topography and is on the order of 10^{-4} m^{-1} in the middepths, much smaller than $1/h \sim 10^{-3}$ m^{-1}. We observe $\langle w_d\rangle > 0$ in all of our simulations. Ignoring the small correction due to changes in the basin area, this implies that the vertical scale of $\langle\kappa\rangle$ is longer than that of the stratification; that is, $\ell_{\langle\kappa\rangle} > h$.

It has been noted previously that the local buoyancy budget in much of the middepths favors downwelling (St. Laurent et al. 2001; Klocker and McDougall 2010; Ferrari et al. 2016). For interior points where $\mathbf{F}_b = -\kappa\nabla b \approx -\kappa b_z\hat{\mathbf{z}}$, the pointwise budget Eq. (4) can be expressed as

$$\frac{w_d}{\kappa} = \frac{\kappa_z}{\kappa} + \frac{b_{zz}}{b_z}. \tag{16}$$

The right side is again a sum of signed inverse length scales. Available observations suggest that κ decays above rough topography over a scale of a few hundred meters, shorter than the vertical scale of the stratification on the order of 1 km (Polzin et al. 1997; Ledwell et al. 2000; St. Laurent et al. 2012; Waterhouse et al. 2014). The right side of Eq. (16) is therefore negative throughout most of the interior of the middepths, implying $w_d < 0$.

There are still locations where Eq. (16) predicts local upwelling. Far above topography where κ approaches a background interior value, κ_z approaches zero, and the familiar constant-κ Munk balance is recovered. Additionally, in bottom boundary layers, b_z becomes much smaller, shortening the vertical scale of the stratification in favor of boundary upwelling—see Ferrari et al. (2016) for a more detailed analysis that accounts for the small lateral gradients expected along boundaries.

The question of why the partitioning of volume fluxes between the upwelling and downwelling regions favors net upwelling in closed basins can be understood in terms of our framework. It comes down to a difference between the decay scales of the pointwise κ as a function of height above bottom and the isopycnal-averaged $\langle\kappa\rangle$ as a function of average isopycnal height. Equation (15) makes it clear that for net upwelling to occur, $\langle\kappa\rangle$ must decay more slowly with height than the stratification does with depth. Computing $\langle\kappa\rangle_z$ suggests why this is plausible even if the pointwise decay of κ above rough topography occurs on shorter scales than the characteristic scale of the stratification.

From the definition of $\langle\kappa\rangle$,

$$\frac{\partial\langle\kappa\rangle}{\partial z} = \frac{\partial}{\partial z}\left(\frac{1}{A}\int_S \kappa\, dS\right) = -\frac{A_z}{A}\langle\kappa\rangle + \frac{1}{A}\frac{\partial}{\partial z}\int_S \kappa\, dS. \tag{17}$$

The derivative of the integral can be expressed via the generalized Leibniz rule as the sum of two terms, one due to changes of κ with z and the other due to the expansion of S with z (see appendix A). Evaluating the derivative and dividing through by $\langle\kappa\rangle$ gives

$$\frac{\langle\kappa\rangle_z}{\langle\kappa\rangle} = -\frac{A_z}{A} + \frac{\langle\kappa_z\rangle}{\langle\kappa\rangle} + \frac{1}{\langle\kappa\rangle A}\oint_{\partial S}\frac{\kappa}{|\nabla D|}\, d\ell, \tag{18}$$

where ∂S is the perimeter of S and $|\nabla D|$ is the slope of the bottom topography. Equation (15) can then be substituted into Eq. (18) to facilitate a direct comparison with the pointwise budget and partition the net transport into interior and boundary components:

$$\frac{\langle w_d\rangle}{\langle\kappa\rangle} = \underbrace{\frac{\langle\kappa_z\rangle}{\langle\kappa\rangle}}_{\text{int down}} + \underbrace{\frac{b_{zz}}{b_z}}_{\text{int up}} + \underbrace{\frac{1}{\langle\kappa\rangle A}\oint_{\partial S}\frac{\kappa}{|\nabla D|}\, d\ell}_{\text{boundary up}}. \tag{19}$$

Equation (19) may appear like a crude average of the pointwise budget Eq. (16) assuming flat isopycnals that extend all the way to the domain boundary, except for the last integral term which proves to be crucial to explain the net upwelling. Indeed the negative contribution of κ_z/κ represents interior downwelling and is larger than the positive contribution b_{zz}/b_z, which represents interior upwelling. The last term captures the along-sloping-boundary upwelling driven by the convergence of the buoyancy fluxes along boundaries to satisfy the no-normal-flux condition—see McDougall and Ferrari (2017) for a detailed discussion of this point. The appearance of this term can be traced back to the derivation of the diapycnal volume transport in section 2a, where care is taken not to discard this boundary layer upwelling.

The boundary layer volume flux can be large enough to reconcile the interior pointwise budget that favors downwelling with our models and observation-based estimates that evince net upwelling. This can be illustrated with scaling analysis. Assuming κ is equal to some large constant κ_0 along the boundary, then

$$\frac{1}{\langle\kappa\rangle A}\oint_{\partial S}\frac{\kappa}{|\nabla D|}\, d\ell = \frac{\kappa_0 A_z}{\langle\kappa\rangle A}. \tag{20}$$

The factor of $\kappa_0/\langle\kappa\rangle$ can be greater than 10, which when multiplied by $A_z/A \sim 10^{-4}$ makes the full boundary upwelling term in Eq. (19) comparable to the other terms, tilting the balance of volume fluxes toward $\langle w_d\rangle > 0$. We see evidence of this in our global model, where $\kappa_0/\langle\kappa\rangle$ ranges from 5 to 20 between 3- and 1-km depth and $\ell_\kappa < h < \ell_{\langle\kappa\rangle}$ is satisfied with $\ell_\kappa = 667$ m, $h = 756$ m, and $\ell_{\langle\kappa\rangle} = 1454$ m.

Importantly, in the middepths it is not the magnitude of the change in basin area, the A_z/A term in Eq. (15), that accounts for the difference in sign between $\langle w_d\rangle$ in Eq. (15) and w_d in Eq. (16) as conjectured in the literature on hypsometric effects (Klocker and McDougall 2010; Polzin and McDougall 2022). Rather it is because of large diffusivities along sloping topography, even in the face of small changes in basin area, that $\langle\kappa\rangle$ can decay much more slowly with height than κ and that the boundary layer upwelling can be strong enough to result in $\langle w_d\rangle > 0$.

The specifics of how the three-dimensional structure of κ affects the basin-averaged profiles of $\langle\kappa\rangle$ and b_z remain to be explored. In particular, the sensitivity of the $\langle\kappa\rangle$ profile to variation in κ_0 or the pointwise structure of κ is unclear. Without running simulations, it is impossible to deduce the exact $\langle\kappa\rangle$ profile corresponding to a particular κ profile. But averaging κ profiles at constant depth as a proxy for $\langle\kappa\rangle$ yields some intuition. Brief experimentation with the data of Nikurashin

and Ferrari (2013), whose κ profiles feature nonuniform bottom values, suggests that $\langle\kappa\rangle$ could still look exponential-like with a decay scale controlled by topography. Further checks with a power-law form for κ as a function of height above bottom as suggested by Polzin (2004) result in similarly exponential $\langle\kappa\rangle$ profiles. It is possible that the topography imposes a sufficiently slow decay of $\langle\kappa\rangle$ such that the distinction between the shapes of exponential, linear, power-law, etc., profiles may be irrelevant to a large-scale description of the stratification. We leave the necessary conditions on κ for the $\langle\kappa\rangle$ profile to support an exponential stratification as a matter for future research.

5. Conclusions

Equation (10) successfully relates the diffusivity, upwelling, and stratification of the middepths for all of the equilibrated model runs tested. Analysis of Eq. (10) demonstrates that $\langle\kappa\rangle$ must vary with depth for both Ψ and N^2 to have magnitudes and vertical structures consistent with observations and estimates. Although estimates of Ψ from hydrography and observations of N^2 allow us to infer the associated profile of $\langle\kappa\rangle$, we lack a theoretical argument to explain our finding that the diapycnal velocity $\langle w_d\rangle$ has the same vertical structure as $\langle\kappa\rangle$, a relationship that our models and observations exhibit and our theory seems to demand. Progress in addressing this question may be possible by extending the theoretical framework developed by Nikurashin and Vallis (2011) to allow for a vertically varying diffusivity.

These results help to settle an ongoing debate about the magnitude of mixing in the deep ocean. Munk's value of 10^{-4} m^2 s^{-1} is often quoted as the mixing required to support the ocean overturning circulation, but observations fail to report such large values a few hundred meters above the ocean floor. Our analysis suggests that this value only applies at the bottom of the middepths, where the average upwelling velocity is at its maximum. Further up in the water column, both the average diffusivity and upwelling of our simulations decay in nearly constant proportion, and the mixing required to support the overturning within the middepths therefore becomes progressively smaller between 3 and 1 km.

In the abyss beneath 3-km depth, isopycnals bend into the seafloor, breaking the flat-isopycnal assumption used to derive Eq. (10). While this may be accounted for by following the procedure outlined in appendix B, the lack of horizontal uniformity in the density structure calls a one-dimensional description into question. Additionally, the presence of progressively more extensive topographic features results in a decrease in the area of deeper isopycnals, an aspect ignored in our analysis of Eq. (10) in section 4a. It is therefore not a surprise that the stratification ceases to be exponential beneath 3 km.

Our results are supported by the completely independent analysis of Lumpkin and Speer (2007), who use an inverse model of the global ocean to infer the overturning circulation and mixing from hydrography and air–sea flux measurements. World Ocean Circulation Experiment (WOCE) sections are used to partition the ocean into boxes, and each box is further divided into 45 density classes. Diffusive fluxes and adjustments to the thermal wind and Ekman flows are computed which achieve consistency with observations, conserve heat, freshwater, and salt, and minimize overall diapycnal mixing. The resulting adjusted thermal wind fields are integrated to produce an overturning circulation Ψ, which is used along with the stratification N^2 obtained directly from hydrography to deduce an effective profile of $\langle\kappa\rangle$. The inverse calculation demands a strongly bottom-enhanced profile of $\langle\kappa\rangle$. As their analysis is carried out entirely in neutral density coordinates, we cannot assess whether the inferred diffusivity profile is well approximated by an exponential function in depth coordinates. Nonetheless, the overall decay of $\langle\kappa\rangle$ above topography accompanied by a concurrent decay in Ψ is fully consistent with our results.

Last, but not least, all of the models in our hierarchy use the Gent–McWilliams parameterization of baroclinic eddies with a constant diffusivity. Yang and Tziperman (2022) show that changes in diapycnal diffusivity affect the rate of baroclinic instability. Future work should therefore explore how this feedback may affect the relationship between Ψ, κ, and N^2. More generally, it would be beneficial to extend the study to more comprehensive, fully equilibrated ocean models.

Acknowledgments. We are thankful for helpful discussions with Carl Wunsch and feedback from two anonymous reviewers that improved this paper. Mason Rogers and Raffaele Ferrari acknowledge support through NSF Awards OCE-1756324 and OCE-1736109. Mason Rogers is additionally supported by the NSF Graduate Research Fellowship Program. Louis-Philippe Nadeau is partly supported through NSERC Award RGPIN-2022-04306. The authors report no conflicts of interest.

Data availability statement. Data required for the computation of the meridional overturning circulation from a state estimate and for the heat and salt forcing of the coarse global model are taken from ECCO version 4 release 3 (Forget et al. 2015; Fukumori et al. 2017), available online (https://ecco.jpl.nasa.gov/drive/files/Version4/Release3/). Observations of the zonally averaged stratification are taken from the WOCE Hydrographic Climatology dataset (Gouretski and Koltermann 2004; https://odv.awi.de/data/ocean/woce-global-hydrographic-climatology/). Data from the idealized and coarse global model configurations are available from the authors (https://github.com/masonrogers14/middepth_data).

APPENDIX A

The Reynolds Transport Theorem

The Reynolds transport theorem, a special case of the generalized Leibniz rule, is used to express the rate of change of an integrated quantity as a sum of contributions due to fluctuations in the quantity and motion of the volume of integration:

$$\frac{d}{dt}\int_{\Omega(t)} f(\mathbf{x}, t)\, dV = \int_{\Omega(t)} \frac{\partial f(\mathbf{x}, t)}{\partial t}\, dV + \int_{\partial\Omega(t)} f(\mathbf{x}, t)\mathbf{v}_b \cdot \hat{\mathbf{n}}\, dS. \tag{A1}$$

Here Ω is a time-dependent domain with boundary $\partial\Omega$ moving at velocity $\mathbf{v}_b$.

However, the changing volume in question need not be indexed by time. For our case, the volume $V(y, b)$ is parameterized by b. The upper boundary $S(y, b)$ is the only one that changes as b changes, and its "velocity" with respect to changes in b is given by

$$\mathbf{v}_b = \frac{\nabla b}{|\nabla b|^2}. \tag{A2}$$

Moreover, the flux divergence $\nabla \cdot \mathbf{F}_b$ does not depend on the position of the upper boundary b. Thus applying Eq. (A1) gives

$$\frac{\partial}{\partial b}\int_{V(y,b)} \nabla \cdot \mathbf{F}_b \, dV = \int_{S(y,b)} (\nabla \cdot \mathbf{F}_b)\frac{\nabla b \cdot \hat{\mathbf{n}}}{|\nabla b|^2} \, dS \tag{A3}$$

Last, the unit normal vector $\hat{\mathbf{n}}$ to $S(y, b)$ is equal to $\nabla b/|\nabla b|$ by definition, yielding

$$\frac{\partial}{\partial b}\int_{V(y,b)} \nabla \cdot \mathbf{F}_b \, dV = \int_{S(y,b)} \frac{\nabla \cdot \mathbf{F}_b}{|\nabla b|} \, dS \tag{A4}$$

or equivalently Eq. (6).

APPENDIX B

An Exact Solution for the Stratification

To solve Eq. (7) for the stratification exactly, we introduce a new vertical coordinate $\overline{z}$ which is a diffusivity-weighted isopycnal depth. Let $\langle\rangle$ denote an isopycnal average and $\langle\rangle_\kappa$ denote a κ-weighted isopycnal average; that is,

$$\langle\phi\rangle \equiv \frac{\int_{S(y,b)} \phi \, dS}{\int_{S(y,b)} dS} \quad \text{and} \quad \langle\phi\rangle_\kappa \equiv \frac{\int_{S(y,b)} \kappa\phi \, dS}{\int_{S(y,b)} \kappa \, dS}. \tag{B1}$$

Note that these averages are taken north of latitude y and hence still depend on a choice of y. We then define $\overline{z}$ via

$$\frac{\partial \overline{z}}{\partial b} \equiv \left\langle \frac{1}{(\partial z/\partial b)} \right\rangle_\kappa^{-1}. \tag{B2}$$

In $\overline{z}$ coordinates, after multiplying by $\partial b/\partial \overline{z}$ Eq. (7) becomes

$$\Psi \frac{\partial b}{\partial \overline{z}} = -\frac{\partial}{\partial \overline{z}}\left(\frac{\partial b}{\partial \overline{z}}\langle\kappa\rangle A\right), \tag{B3}$$

where A is the area of $S(y, b)$. If the diapycnal transport Ψ and an initial condition $b_{\overline{z}}(\overline{z}_0)$ are known, the exact solution to Eq. (B3) can be written as

$$b_{\overline{z}} = b_{\overline{z}}(\overline{z}_0)\frac{(\langle\kappa\rangle A)|_{\overline{z}=\overline{z}_0}}{\langle\kappa\rangle A} \exp\left[-\int_{\overline{z}_0}^{\overline{z}} \frac{\Psi}{\langle\kappa\rangle A} d\overline{z}'\right]. \tag{B4}$$

Equation (B4) is most useful to predict the observed stratification if $b_{\overline{z}}$ is a good approximation of the z-coordinate stratification b_z. Because isopycnals in the middepth Indo-Pacific are nearly flat as shown in Fig. 1, the dependence of the middepth stratification on y is weak, and $b_z \approx b_{\overline{z}}$. We therefore ignore the distinction between $\overline{z}$ and z in our analysis of Eq. (B4), which leaves Eq. (10). This approximation is invalid closer to bottom topography, where the role of correlations between κ and b_z is more important (Drake et al. 2020).

REFERENCES

Cessi, P., 2019: The global overturning circulation. *Annu. Rev. Mar. Sci.*, **11**, 249–270, https://doi.org/10.1146/annurev-marine-010318-095241.

Drake, H. F., R. Ferrari, and J. Callies, 2020: Abyssal circulation driven by near-boundary mixing: Water mass transformations and interior stratification. *J. Phys. Oceanogr.*, **50**, 2203–2226, https://doi.org/10.1175/JPO-D-19-0313.1.

Ferrari, R., A. Mashayek, T. J. McDougall, M. Nikurashin, and J.-M. Campin, 2016: Turning ocean mixing upside down. *J. Phys. Oceanogr.*, **46**, 2239–2261, https://doi.org/10.1175/JPO-D-15-0244.1.

Forget, G., J.-M. Campin, P. Heimbach, C. N. Hill, R. M. Ponte, and C. Wunsch, 2015: ECCO version 4: An integrated framework for non-linear inverse modeling and global ocean state estimation. *Geosci. Model Dev.*, **8**, 3071–3104, https://doi.org/10.5194/gmd-8-3071-2015.

Fukumori, I., O. Wang, I. Fenty, G. Forget, P. Heimbach, and R. M. Ponte, 2017: ECCO version 4 release 3. Tech. Rep., 10 pp., https://dspace.mit.edu/bitstream/handle/1721.1/110380/ECCO-version4-release3-summary.pdf?sequence=1&isAllowed=y.

Gent, P. R., and J. C. McWilliams, 1990: Isopycnal mixing in ocean circulation models. *J. Phys. Oceanogr.*, **20**, 150–155, https://doi.org/10.1175/1520-0485(1990)020<0150:IMIOCM>2.0.CO;2.

Gerdes, R., C. Köberle, and J. Willebrand, 1991: The influence of numerical advection schemes on the results of ocean general circulation models. *Climate Dyn.*, **5**, 211–226, https://doi.org/10.1007/BF00210006.

Gnanadesikan, A., 1999: A simple predictive model for the structure of the oceanic pycnocline. *Science*, **283**, 2077–2079, https://doi.org/10.1126/science.283.5410.2077.

Gouretski, V., and K. Koltermann, 2004: WOCE Global Hydrographic Climatology. BSH Tech. Rep. 35, 52 pp., www.bsh.de/de/Produkte/Buecher/Berichte_/Bericht35/Bericht1.pdf.

Jackett, D. R., and T. J. McDougall, 1995: Minimal adjustment of hydrographic profiles to achieve static stability. *J. Atmos. Oceanic Technol.*, **12**, 381–389, https://doi.org/10.1175/1520-0426(1995)012<0381:MAOHPT>2.0.CO;2.

Klocker, A., and T. J. McDougall, 2010: Influence of the nonlinear equation of state on global estimates of dianeutral advection and diffusion. *J. Phys. Oceanogr.*, **40**, 1690–1709, https://doi.org/10.1175/2010JPO4303.1.

Ledwell, J. R., A. J. Watson, and C. S. Law, 1998: Mixing of a tracer in the pycnocline. *J. Geophys. Res.*, **103**, 21 499–21 529, https://doi.org/10.1029/98JC01738.

——, E. T. Montgomery, K. L. Polzin, L. C. St. Laurent, R. W. Schmitt, and J. M. Toole, 2000: Evidence for enhanced mixing over rough topography in the abyssal ocean. *Nature*, **403**, 179–182, https://doi.org/10.1038/35003164.

——, L. C. St. Laurent, J. B. Girton, and J. M. Toole, 2011: Diapycnal mixing in the Antarctic Circumpolar Current. *J. Phys. Oceanogr.*, **41**, 241–246, https://doi.org/10.1175/2010JPO4557.1.

Liang, X., M. Spall, and C. Wunsch, 2017: Global ocean vertical velocity from a dynamically consistent ocean state estimate. *J. Geophys. Res. Oceans*, **122**, 8208–8224, https://doi.org/10.1002/2017JC012985.

Lin, X., X. Zhai, Z. Wang, and D. R. Munday, 2018: Mean, variability, and trend of Southern Ocean wind stress: Role of wind fluctuations. *J. Climate*, **31**, 3557–3573, https://doi.org/10.1175/JCLI-D-17-0481.1.

Lumpkin, R., and K. Speer, 2007: Global ocean meridional overturning. *J. Phys. Oceanogr.*, **37**, 2550–2562, https://doi.org/10.1175/JPO3130.1.

Marshall, J., and T. Radko, 2003: Residual-mean solutions for the Antarctic Circumpolar Current and its associated overturning circulation. *J. Phys. Oceanogr.*, **33**, 2341–2354, https://doi.org/10.1175/1520-0485(2003)033<2341:RSFTAC>2.0.CO;2.

——, C. Hill, L. Perelman, and A. Adcroft, 1997: Hydrostatic, quasi-hydrostatic, and nonhydrostatic ocean modeling. *J. Geophys. Res.*, **102**, 5733–5752, https://doi.org/10.1029/96JC02776.

——, D. Jamous, and J. Nilsson, 1999: Reconciling thermodynamic and dynamic methods of computation of water-mass transformation rates. *Deep-Sea Res. I*, **46**, 545–572, https://doi.org/10.1016/S0967-0637(98)00082-X.

Mashayek, A., R. Ferrari, M. Nikurashin, and W. R. Peltier, 2015: Influence of enhanced abyssal diapycnal mixing on stratification and the ocean overturning circulation. *J. Phys. Oceanogr.*, **45**, 2580–2597, https://doi.org/10.1175/JPO-D-15-0039.1.

McDougall, T. J., and P. M. Barker, 2011: Getting started with TEOS-10 and the Gibbs Seawater (GSW) oceanographic toolbox. SCOR/IAPSO WG127, 34 pp., https://www.teos-10.org/pubs/Getting_Started.pdf.

——, and R. Ferrari, 2017: Abyssal upwelling and downwelling driven by near-boundary mixing. *J. Phys. Oceanogr.*, **47**, 261–283, https://doi.org/10.1175/JPO-D-16-0082.1.

Miller, M. D., X. Yang, and E. Tziperman, 2020: Reconciling the observed mid-depth exponential ocean stratification with weak interior mixing and Southern Ocean dynamics via boundary-intensified mixing. *Eur. Phys. J. Plus*, **135**, 375, https://doi.org/10.1140/epjp/s13360-020-00375-y.

Munday, D. R., H. L. Johnson, and D. P. Marshall, 2013: Eddy saturation of equilibrated circumpolar currents. *J. Phys. Oceanogr.*, **43**, 507–532, https://doi.org/10.1175/JPO-D-12-095.1.

Munk, W., and C. Wunsch, 1998: Abyssal recipes II: Energetics of tidal and wind mixing. *Deep-Sea Res. I*, **45**, 1977–2010, https://doi.org/10.1016/S0967-0637(98)00070-3.

Munk, W. H., 1966: Abyssal recipes. *Deep-Sea Res. Oceanogr. Abstr.*, **13**, 707–730, https://doi.org/10.1016/0011-7471(66)90602-4.

Nikurashin, M., and G. Vallis, 2011: A theory of deep stratification and overturning circulation in the ocean. *J. Phys. Oceanogr.*, **41**, 485–502, https://doi.org/10.1175/2010JPO4529.1.

——, and R. Ferrari, 2013: Overturning circulation driven by breaking internal waves in the deep ocean. *Geophys. Res. Lett.*, **40**, 3133–3137, https://doi.org/10.1002/grl.50542.

Orsi, A. H., and T. Whitworth III, 2005: *Southern Ocean*. Vol. 1, *Hydrographic Atlas of the World Ocean Circulation Experiment (WOCE)*, M. Sparrow, P. Chapman, and J. Gould, Eds., International WOCE Project Office, 223 pp., https://doi.org/10.21976/C6BC78.

Polzin, K., 2004: Idealized solutions for the energy balance of the finescale internal wave field. *J. Phys. Oceanogr.*, **34**, 231–246, https://doi.org/10.1175/1520-0485(2004)034<0231:ISFTEB>2.0.CO;2.

Polzin, K. L., and T. J. McDougall, 2022: Mixing at the ocean's bottom boundary. *Ocean Mixing*, M. Meredith and A. Naveira Garabato, Eds., Elsevier, 145–180, https://doi.org/10.1016/B978-0-12-821512-8.00014-1

——, J. M. Toole, J. R. Ledwell, and R. W. Schmitt, 1997: Spatial variability of turbulent mixing in the abyssal ocean. *Science*, **276**, 93–96, https://doi.org/10.1126/science.276.5309.93.

Redi, M. H., 1982: Oceanic isopycnal mixing by coordinate rotation. *J. Phys. Oceanogr.*, **12**, 1154–1158, https://doi.org/10.1175/1520-0485(1982)012<1154:OIMBCR>2.0.CO;2.

Rousselet, L., P. Cessi, and G. Forget, 2021: Coupling of the mid-depth and abyssal components of the global overturning circulation according to a state estimate. *Sci. Adv.*, **7**, eabf5478, https://doi.org/10.1126/sciadv.abf5478.

St. Laurent, L. C., J. M. Toole, and R. W. Schmitt, 2001: Buoyancy forcing by turbulence above rough topography in the abyssal Brazil Basin. *J. Phys. Oceanogr.*, **31**, 3476–3495, https://doi.org/10.1175/1520-0485(2001)031<3476:BFBTAR>2.0.CO;2.

——, H. L. Simmons, and S. R. Jayne, 2002: Estimating tidally driven mixing in the deep ocean: Estimating tidally driven mixing. *Geophys. Res. Lett.*, **29**, 2106, https://doi.org/10.1029/2002GL015633.

St. Laurent, L., A. C. Naveira Garabato, J. R. Ledwell, A. M. Thurnherr, J. M. Toole, and A. J. Watson, 2012: Turbulence and diapycnal mixing in drake passage. *J. Phys. Oceanogr.*, **42**, 2143–2152, https://doi.org/10.1175/JPO-D-12-027.1.

Talley, L. D., 2007: *Pacific Ocean*, Vol. 2, *Hydrographic Atlas of the World Ocean Circulation Experiment (WOCE)*, M. Sparrow, P. Chapman, and J. Gould, Eds., International WOCE Project Office, 326 pp., https://doi.org/10.21976/C6WC77.

——, J. L. Reid, and P. E. Robbins, 2003: Data-based meridional overturning streamfunctions for the global ocean. *J. Climate*, **16**, 3213–3226, https://doi.org/10.1175/1520-0442(2003)016<3213:DMOSFT>2.0.CO;2.

Trenberth, K. E., J. G. Olson, and W. G. Large, 1989: A global ocean wind stress climatology based on ECMWF analyses. NCAR Tech. Note NCAR/TN-338+STR, 93 pp., https://doi.org/10.5065/D6ST7MR9.

Walin, G., 1982: On the relation between sea-surface heat flow and thermal circulation in the ocean. *Tellus*, **34A**, 187–195, https://doi.org/10.3402/tellusa.v34i2.10801.

Waterhouse, A. F., and Coauthors, 2014: Global patterns of diapycnal mixing from measurements of the turbulent dissipation rate. *J. Phys. Oceanogr.*, **44**, 1854–1872, https://doi.org/10.1175/JPO-D-13-0104.1.

Wolfe, C. L., and P. Cessi, 2009: Overturning circulation in an eddy-resolving model: The effect of the pole-to-pole temperature gradient. *J. Phys. Oceanogr.*, **39**, 125–142, https://doi.org/10.1175/2008JPO3991.1.

Yang, X., and E. Tziperman, 2022: The vertical middepth ocean density profile: An interplay between Southern Ocean dynamics and interior vertical diffusivity. *J. Phys. Oceanogr.*, **52**, 2479–2492, https://doi.org/10.1175/JPO-D-21-0188.1.